**Advanced Steel Construction** – Vol. 20 No. 2 (2024) 179–187
**DOI:**10.18057/IJASC.2024.20.2.10
(Special Issue: *11st International Conference on Advances in Steel Structures, ICASS'2023, Kuching, Sarawak, Malaysia*)


# INFLUENCE OF SECTION SLENDERNESS ON THE AXIAL PERFORMANCE OF HIGH-STRENGTH COLD-FORMED STEEL BUILT-UP COLUMNS

Shin-Rui Kho [1], Adeline LingYing Ng [1,*], Hieng-Ho Lau [1], Emad Gad [2] and Krishanu Roy [3]

[1] *Faculty of Engineering, Computing and Science, Swinburne University of Technology (Sarawak Campus), Kuching 93350, Malaysia*
[2] *School of Engineering, Swinburne University of Technology, Hawthorn 3122, Australia*
[3] *School of Engineering Academic, University of Waikato, Hamilton 3216, New Zealand*
** (Corresponding author: E-mail: ang@swinburne.edu.my)*

**ABSTRACT**

Cold-formed steel (CFS) sections are widely utilised in roofing and framing systems due to their lightweight properties and ease of fabrication and construction. The application of CFS built-up sections was introduced to enhance the strength and stability of single channels. However, typical CFS channels possess slender profiles with a high section slenderness ratio $(w/t)_{max}$, making them susceptible to buckling and limiting their effectiveness. Consequently, this study examined the axial compression behaviour and cost-effectiveness of G550 high-strength CFS built-up sections with a reduced $(w/t)_{max}$ compared to conventional industry sizes. Experimental and numerical studies were conducted to assess the effect of member slenderness $(KL/r)_m$ and screw arrangement on the CFS built-up sections with different section slenderness. The results demonstrated that the proposed sections, with a lower $(w/t)_{max}$, significantly improved buckling resistance for members with $(KL/r)_m$ less than 90. This improvement is attributed to their more compact profile design, which restrained the occurrence of local buckling. Furthermore, these sections were found to be more cost-effective, offering greater strength at a reduced weight.

**ARTICLE HISTORY**

Received: 18 June 2024
Revised: 18 June 2024
Accepted: 18 June 2024

**KEYWORDS**

Axial compression;
High-strength cold-formed steel;
Slenderness ratios;
Screw arrangement;
Buckling resistance;
Cost-effectiveness



## 1. Introduction

The application of cold-formed steel (CFS) gained popularity due to its light gauge properties while achieving impressive performance [1-3]. However, the slender geometry layout makes it prone to buckling and leads to high instability of structural members [1,4-5]. Therefore, CFS built-up sections were introduced to enhance the load-carrying capacity and stability of single channels, and these sections are commonly applied in various types of structural members such as roof and wall systems, portal frames, columns, and beams [6-7]. Past research investigated the structural performance of various types of CFS built-up sections with different arrangements of CFS sections. The typical CFS built-up sections investigated in the past are shown in Fig. 1. Fig. 1(a) shows the typical CFS single channels applied in structural design and used to form the built-up sections. Moreover, Fig. 1(b) presented the different types of CFS built-up sections that have been investigated in previous research which include open built-up sections, closed built-up sections, built-up battened sections, built-up gapped sections, and other built-up sections (hybrid built-up section, multi-limbs built-up section, built-up hollow flange section, half-open built-up section, and cruciform built-up section). Notably, most of the studies mentioned above were conducted to investigate the axial capacity of built-up sections formed using existing CFS channels in the industry with a maximum width-to-thickness ratio, $(w/t)_{max}$ of 45 and above. A summary of the axial performance of CFS open built-up sections with different slenderness ratios is shown in Fig. 2 [8-15]. The axial capacity ($P_u$) in Fig. 2 was normalised by multiplying the ultimate tensile strength ($f_u$) and gross cross-sectional area ($A_g$) of the investigated sections for comparison to account for different material grades and section sizes.

It is more practical to form the built-up sections using the common sizes of CFS channels. However, the sections do not achieve full capacity as the normalised capacity was not close to the unity shown in Fig. 2, indicating that the section was not fully effective. As CFS channels have a slender profile that leads to high instability and is prone to buckle, a smaller $(w/t)_{max}$ is expected to enhance the buckling resistance and make the CFS sections more effective. Several research investigated the axial compression performance of CFS open built-up columns with different cross-section dimensions [10-15], but the effect of section slenderness was not discussed. Yet, Zhou et al. [12] claimed that the section slenderness was an important parameter that influences the capacity of the CFS built-up sections. Although many research was conducted, the axial behaviour of the CFS sections with the $(w/t)_{max}$ lesser than 45 is rarely explored, therefore the structural performance of the built-up sections fabricated using a small $(w/t)_{max}$ is worth examining. Apart from that, a reduced size of CFS sections is potentially more cost-effective if it can achieve a similar capacity to common CFS sections while utilising lesser materials. Furthermore, Vy and Mahendran [13] studied the effect of screw arrangement on the CFS open lipped built-up sections fabricated using common CFS sections. The axial compression capacity of the specimens with double rows fasteners was increased by an average of 4% compared to single row fasteners and the increase is relatively significant for slender columns. Meanwhile, the influence of the screw arrangement is unexplored for the built-up members with section slenderness lesser than 45. Therefore, this study aims to investigate the axial compression behaviour of CFS built-up columns fabricated with a $(w/t)_{max}$ ranging from 41 to 45. An experimental testing programme was carried out for 12 open lipped built-up columns with different member lengths ($L$) and screw spacing ($a$). Following this, finite element (FE) models were developed and validated using the experimental data. Finally, parametric studies were performed to examine further the effect of modified slenderness ratio $(KL/r)_m$ and screw arrangement on the proposed sections.

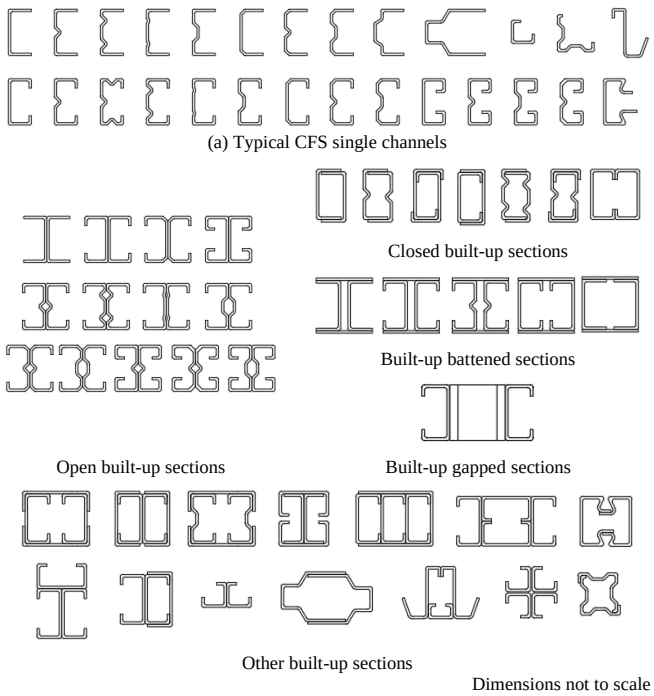


**Fig. 1** Various types of CFS built-up sections investigated in past research

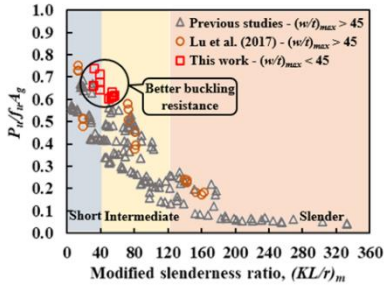


**Fig. 2** Axial performance of CFS open built-up columns with different slenderness ratios

## 2. Experimental testing

### *2.1. Test specimens*

The test programme consists of 12 sets of specimens fabricated with two scaled-down lipped channels connected back-to-back with self-drilling screws. The lipped channels were press braked from a 1 mm thick plain steel sheet with a nominal yield strength of 550 MPa with a nominal bend radius, *R* of 2.5 mm. The lipped channel was designed with a nominal width of 51 mm web *(h)*, 20 mm flange *(b)* and 10 mm lip *(d)* as shown in Fig. 3(a). The element widths of the proposed sections were scaled down with a $(w/t)_{max}$ ranging from 41 to 45. A single row of screws was designed to fasten the CFS channels to achieve good coupling conditions between the fastened sections. In addition, Gauge 12 self-drilling screws were used as the connector between the channels with a 50 mm end distance and two different intermediate screw spacings of 100 mm and 200 mm along the longitudinal direction. The dimensions of the self-drilling screw were presented in Fig. 3(b) with a diameter of 5.35 mm and a length of drill point 7 mm. Then, the measured dimensions for each specimen were indicated in Table 1. Prior to conducting the experimental testing, every specimen was labelled to indicate the sectional profile and the corresponding design parameters as shown in Fig. 3(c). The investigated built-up section was given a series name which is open lipped (OL) series and further differentiated into S100 and S200 series for different screw spacings.

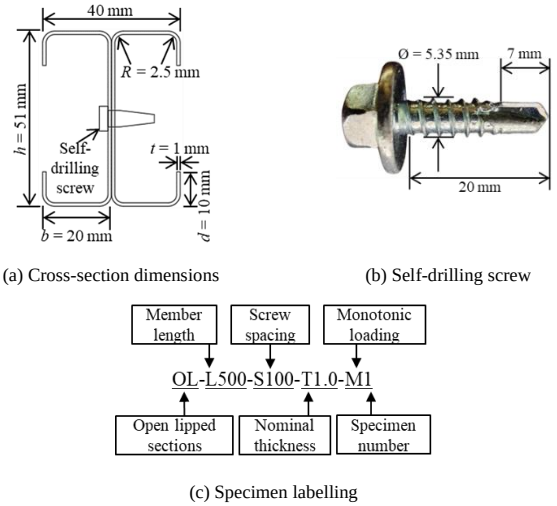


(a) Cross-section dimensions (b) Self-drilling screw

(c) Specimen labelling

**Fig. 3** Detailed of proposed sections

**Table 1**
Measured specimen dimensions and parameters

| Classification | Specimen | | *h* (mm) | *b* (mm) | *d* (mm) | *t* (mm) | *L* (mm) | *a* (mm) | $(w/t)_{max}$ | $(KL/r)_m$ | $A_g$ (mm²) | $\delta$ |
|---|---|---|---|---|---|---|---|---|---|---|---|---|
| S100 series | | | | | | | | | | | | |
| Short | OL-L300-S100-T1.0 | M1 | 51.58 | 19.09 | 10.38 | 1.03 | 297 | 100 | 43.22 | 32.48 | 208.52 | 0.9 |
| | | M2 | 51.63 | 19.41 | 10.50 | 1.00 | 298 | 100 | 44.63 | 31.90 | 204.60 | |
| | | M3 | 51.59 | 19.79 | 10.00 | 1.06 | 299 | 100 | 41.95 | 31.76 | 215.66 | |
| Intermediate | OL-L500-S100-T1.0 | M1 | 51.79 | 18.59 | 11.08 | 1.04 | 501 | 100 | 42.99 | 52.30 | 211.71 | 0.7 |
| | | M2 | 52.17 | 19.75 | 11.02 | 1.04 | 504 | 100 | 43.36 | 49.54 | 217.08 | |
| | | M3 | 51.75 | 18.38 | 11.11 | 1.04 | 504 | 100 | 42.95 | 53.17 | 210.88 | |
| S200 series | | | | | | | | | | | | |
| Short | OL-L300-S200-T1.0 | M1 | 51.20 | 19.52 | 9.94 | 1.00 | 298 | 198 | 44.20 | 39.26 | 201.94 | 0.7 |
| | | M2 | 52.03 | 19.54 | 10.71 | 1.06 | 299 | 199 | 42.37 | 38.99 | 218.55 | |
| | | M3 | 51.98 | 19.67 | 10.49 | 1.05 | 299 | 199 | 42.74 | 38.87 | 216.10 | |
| Intermediate | OL-L500-S200-T1.0 | M1 | 52.06 | 19.79 | 11.27 | 1.04 | 505 | 200 | 43.25 | 54.06 | 218.06 | 0.9 |
| | | M2 | 51.88 | 18.70 | 11.17 | 1.04 | 500 | 200 | 43.08 | 56.92 | 212.73 | |
| | | M3 | 52.47 | 19.63 | 11.07 | 1.04 | 503 | 200 | 43.64 | 54.65 | 217.41 | |

### *2.2. Material properties*

The actual mechanical properties of the components, G550 steel sheets and self-drilling screws were determined by conducting the tensile coupon tests and screw shear tests in accordance with AS/NZS 4600:2018 [16]. Then, the test procedures of tensile coupon tests have been accounted for further considerations recommended in AS1391 [17] and Huang and Young [18]. A slow loading rate recommended for research purposes was adopted to obtain accurate mechanical properties of the steel materials. The measured stress-strain behaviour of steel and the shear behaviour of screw were summarised in Fig. 4 and used as constitutive models to apply the actual properties of the components to numerical models.

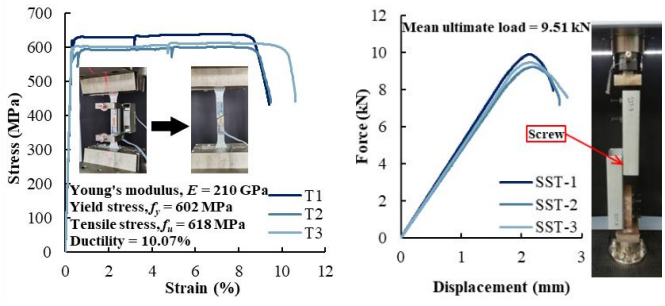


(a) Tensile coupon test results (b) Screw shear test results

**Fig. 4** Material properties

### 2.3. Dimension and geometric imperfection measurements

All 12 specimens were measured before tests. The dimension measurement included the elements of web ($h$), flange ($b$), lip ($d$), thickness ($t$), member length ($L$), and intermediate screw spacing ($a$) and the measured data was listed in Table 1. The fabrication, installation, and transportation processes of the CFS specimen potentially caused geometric imperfections. Therefore, the initial global and local imperfections were also measured from the data point location indicated in Fig. 5. The global imperfection was measured at the mid-height of the specimen, while local imperfection was measured between the 200 mm central length with a 10 mm interval. Additionally, the datum points were controlled as zero for every measurement to ensure consistency. Then, the measured absolute maximum imperfection magnitudes ($\delta$) were recorded in Table 1 which were the sum of absolute maximum global and local imperfections for each series.

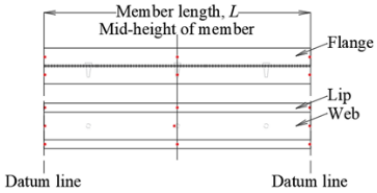


(a) Global imperfection

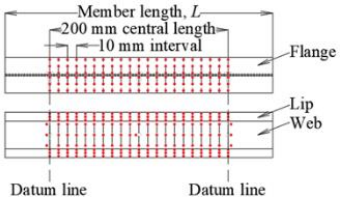


(b) Local imperfection

**Fig. 5** Geometric imperfection measurement

### 2.4. Test setup and operation

The boundary conditions of the built-up columns were designed as pin-ended supports. Two supporting test rigs were specially fabricated to provide the pin-ended boundary condition of the specimens, which only allowed the rotation about the minor axis of the specimens. To ensure full contact between the specimen and the supports, both ends of each specimen are welded to 16 mm thick steel end plates before the test. The schematic diagram and fabricated fixtures of the test setup are shown in Fig. 6.

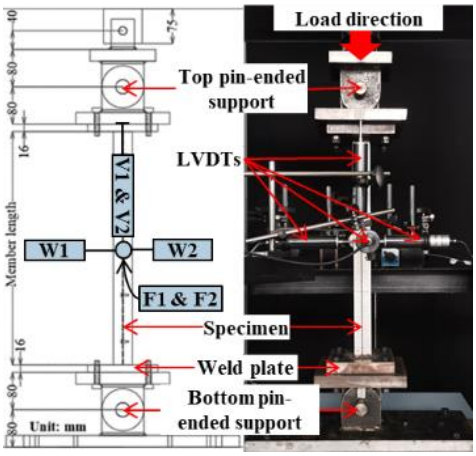


(a) Schematic diagram (b) Actual setup

**Fig. 6** Test setup

Besides, the axial shortening and out-of-plane deformation were measured during the test using the linear variable displacement transducer (LVDT). Two LVDTs were set vertically at the middle of the top plate to determine the axial shortening of the specimen. Additionally, four LVDTs were used to measure the out-of-plane deformation for intermediate columns. Two LVDTs measured the displacement of the web elements while the other two LVDTs measured the displacement at the flanges. Nevertheless, only the out-of-plane deformation at the web elements was measured for short columns due to space limitations.

Since CFS is a strong material with relatively low ductility and the expected displacement before buckling is small, a displacement-controlled loading protocol was used to conduct the monotonic compression test. To determine the static response of the CFS built-up sections, a constant loading rate (0.2 mm/min) was selected to perform the test. A 1 kN preload was applied before executing the actual test to eliminate the gaps between test rigs and the specimen, ensuring uniform axial compression applied on the specimen. The test was terminated after a 20% drop in ultimate load was observed.

### 2.5. Experiment results

The test results are summarised in Table 2 and the observed axial behaviours are presented in Figs. 7 and 8. Based on the analysis, the axial behaviours of the investigated specimens were classified into three stages, which are yield point, ultimate point, and failure point. The yield point of each specimen was determined by using the equivalent elasto-plastic energy absorption method [19]. The ultimate point was identified when the peak load was achieved, while the failure point was measured at a 20% drop in the peak load.

#### 2.5.1. Load-displacement behaviour and failure modes

All tested specimens behaved similarly throughout the test with no significant responses occurring at the elastic stage. Distortional buckling occurred once the applied load surpassed the yield point as indicated in Fig. 7 (refer to the axial shortening) while no local buckling was observed at this stage which may be restrained by their compact cross-section design. Other buckling modes were observed beyond the ultimate point (refer to the out-of-plane deformation). For short columns, local buckling and crushing were observed. The final failure mode was the interactive local-distortional buckling mode, including crushing at the specimen ends. Except for OL-L300-S200-T1.0-M2, no distortional buckling was observed due to the high initial imperfection in the specimen. Meanwhile, for intermediate columns, interactive local-distortional-global buckling was observed. Besides, there was a significant increase in out-of-plane deformation beyond the ultimate point due to the loss of stability of the member. The failure modes of investigated specimens at the failure point are shown in Fig. 8.

**Table 2**
Summary of experimental results

| Specimen | | $P_y$ (kN) | $\Delta_y$ (mm) | $P_u$ (kN) | $\Delta_u$ (mm) | $P_u/f_uA_g$ | Buckling mode | |
|---|---|---|---|---|---|---|---|---|
| | | | | | | | Ultimate | Failure |
| S100 Series | | | | | | | | |
| OL-L300-S100-T1.0 | M1 | 90.38 | 0.88 | 95.05 | 1.04 | 0.74 | D | LDC |
| | M2 | 77.96 | 0.74 | 83.63 | 0.96 | 0.87 | D | LD |
| | M3 | 83.51 | 0.80 | 88.16 | 0.98 | 0.94 | D | LDC |
| OL-L500-S100-T1.0 | M1 | 77.67 | 1.15 | 79.96 | 1.25 | 0.61 | D | DG |
| | M2 | 75.52 | 1.15 | 80.94 | 1.41 | 0.60 | D | LDG |
| | M3 | 77.41 | 1.04 | 79.32 | 1.11 | 0.61 | D | LDG |
| S200 series | | | | | | | | |
| OL-L300-S200-T1.0 | M1 | 84.43 | 0.83 | 88.74 | 1.01 | 0.71 | D | LD |
| | M2 | 82.72 | 0.79 | 87.03 | 0.99 | 0.64 | D | LDC |
| | M3 | 85.49 | 0.78 | 90.29 | 0.92 | 0.68 | D | LDC |
| OL-L500-S200-T1.0 | M1 | 81.72 | 1.20 | 85.12 | 1.30 | 0.63 | D | LDG |
| | M2 | 78.29 | 1.15 | 81.01 | 1.29 | 0.62 | D | LDG |
| | M3 | 78.31 | 1.21 | 82.48 | 1.50 | 0.61 | D | LDG |

Note: D = distortional buckling, LD = interactive local-distortional buckling, LDC = interactive local-distortional buckling with crushing, LDG = interactive local-distortional-global buckling.

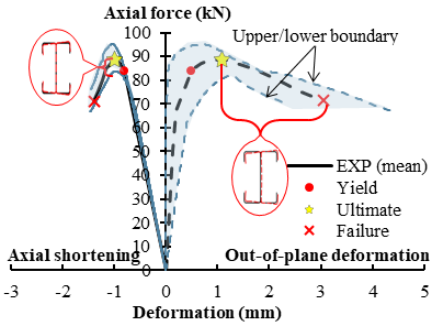


(a) OL-L300-S100-T1.0

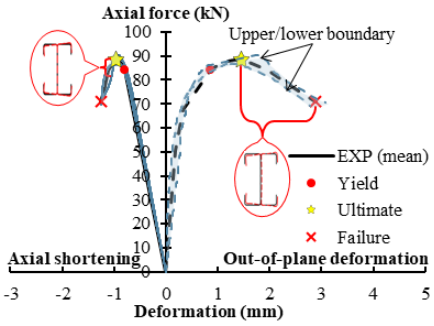


(b) OL-L300-S200-T1.0

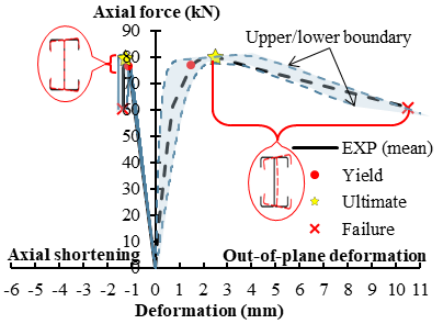


(c) OL-L500-S100-T1.0

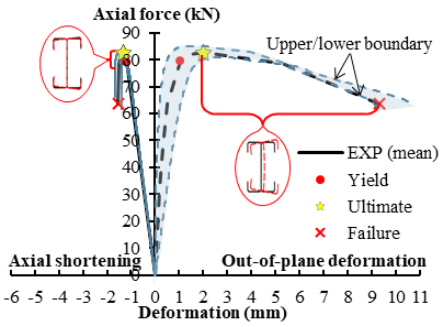


(d) OL-L500-S200-T1.0

**Fig. 7** Experimental results of OL series

*2.5.2. Composite action of built-up columns*

Based on the failure modes in Fig. 8, the composite action of built-up columns was developed as the two channels deformed simultaneously. Besides, no separation of channels and failure at the screw connection was observed. The designed screw arrangement provided a good coupling effect although the intermediate columns with 200 mm screw spacing do not meet the recommended limit of screw spacing in AS/NZS 4600:2018 [20]. Only the short columns with 200 mm screw spacing buckled individually, as predicted in the design codes. It was also found that the investigated specimens achieved greater buckling resistance compared to specimens studied in previous research. As shown in Fig. 2, the normalised axial capacity is closer to unity, which means the proposed sections are more effective.

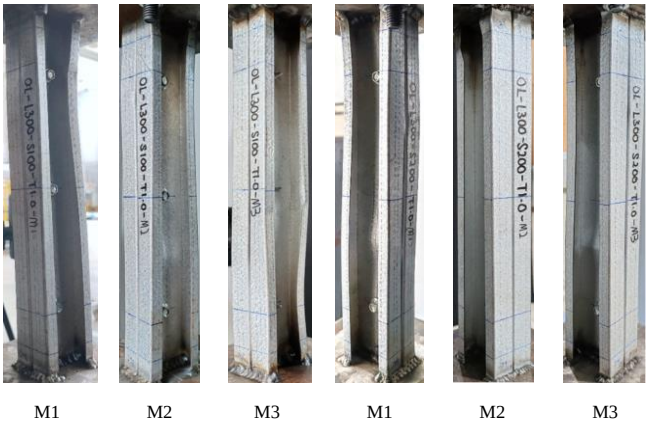

M1 M2 M3 M1 M2 M3

(a) OL-L300-S100-T1.0 (b) OL-L300-S200-T1.0

M1 M2 M3 M1 M2 M3

(c) OL-L500-S100-T1.0 (d) OL-L500-S200-T1.0

**Fig. 8** Failure modes of OL series at failure point

## 3. Numerical simulation

*3.1. Finite element model development*

As the experimental testing was limited to short and intermediate columns, the axial behaviour of slender columns investigated was referred to Lu et al. [10]. The reported failure mode was pure global buckling for all slender built-up columns fabricated using lipped channels with $(w/t)_{max}$ ranging from 71.5 to 93. Therefore, the numerical model was verified and used to perform parametric studies in order to further examine the influence of section slenderness. The respective specimens were named LU series to ease the comparisons with the OL series (proposed section in this study).

*3.1.1. Types of element and mesh*

The CFS specimens were modelled according to their actual dimensions and assigned deformable shell elements type S4R5, in ABAQUS [21]. The mesh size adopted was 5 mm following mesh convergence studies to provide accurate and efficient FEA.

*3.1.2. Material modelling*

The material properties used to simulate the reference specimens were obtained from the experimental results of tensile coupon tests discussed in Section 2.2 and reported data in [10] for the OL series and LU series respectively. The engineering stress-strain curves were converted to true stress-strain curves. Then, the details of elasticity, plasticity, and ductile damage which were required to incorporate into FE models were determined based on the true stress-strain curves.

Furthermore, the screw position and arrangement assigned to FE models

were also according to the measured intermediate screw spacing and arrangement design such as single row screws for the OL series and double rows screws for the LU series. The screw properties were initially assumed as rigid and damage was considered upon reaching the mean ultimate shear capacity determined from the screw shear test. The damage initiation and evolution limits were set as the mean ultimate shear capacity and allowable deformation from the ultimate to the failure point.

*3.1.3. Modelling of initial geometric imperfections*

Furthermore, CFS sections commonly contain geometric imperfections caused during fabrication and transportation processes. These imperfections initiated out-of-straightness and small deflection, weakening the structural members' strength and stiffness [22,23]. Therefore, the measured initial geometric imperfection magnitudes were incorporated into the FE models.

*3.1.4. Boundary conditions*

The numerical models were assigned with the same pin-ended restraints as during experimental testing at both ends to achieve high-accuracy simulation. First, reference points (RPs) were generated at the centroid of the CFS built-up column at both ends. Then, all degrees of freedom (DOF) of the elements (web, flanges, and lips) of the CFS sections were constrained to the RPs using coupling type constraints. For the OL series, all the translational and rotational DOF were fully fixed at both RPs except the rotational DOF of the minor axis at both RPs and the axial translational DOF at the top RP, which was used to apply the displacement loading and to allow the vertical deformation of specimens. Meanwhile, the boundary conditions assigned to the LU series were similar to the OL series with an additional rotational release of the major axis at both RPs for the bidirectionally hinged supports. The assigned boundary conditions for each series are indicated in Fig. 9.

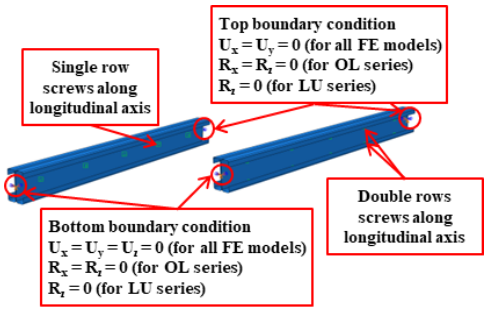


(a) Single row screw (b) Double rows screws

**Fig. 9** Boundary conditions of FE models

*3.1.5. Modelling techniques and loading procedure*

The FEA involved two steps using different solution techniques. Firstly, an Eigenvalue buckling analysis was conducted using linear perturbation analysis to obtain the buckling shape and to incorporate the imperfection of the CFS specimens into the nonlinear models. A concentrated point load was applied at the top end of the specimen to simulate experimental testing conditions. Then, the measured maximum absolute initial imperfection was used as the magnitude and assigned to the lowest-order eigenmodes to model the initial state of the specimen of collapse analysis. Secondly, a nonlinear static analysis was utilised to load the specimen to failure. The nonlinear model was duplicated from the first model (eigenvalue buckling model) to ensure consistency of the utilised cross-sectional dimensions and other parameters throughout the entire FEA. To optimise the convergence issues, an automatic stabilization technique was adopted in this study, which can efficiently obtain a solution in the post-collapse stage with the help of artificial damping. The dissipated energy fraction and the ratio of stabilization to strain energy were set as 0.0002 and 0.05, respectively. Then, the loading protocol assigned in this step was displacement-controlled, which applies the final axial shortening obtained from experimental results at the top RP in the vertical direction to simulate the axial loading acting on the specimens.

*3.2. Mesh convergence and independence study*

Mesh convergence and independence studies were performed to examine the efficiency of the developed FE models. For the OL series, the study and analysis were completed by executing the FEA on the intermediate column with different mesh densities of 2 mm, 3 mm, 4 mm, 5 mm, 8 mm, 10 mm, and 20 mm. The comparisons of the outcomes are presented in Fig. 10. Only the failure mode of the FE model with a 5 mm mesh size was presented as it is the best-fit model. A 5 mm mesh size was selected for both short and intermediate models. A similar process was conducted for the LU series, both intermediate and slender columns were selected specimens to conduct this study. The intermediate column was validated again to ensure the 5 mm mesh size is still valid for the section size with greater section slenderness. It was found that a 5 mm mesh size is suitable for the intermediate column, while 8 mm is more efficient for slender columns presented in Fig. 11.

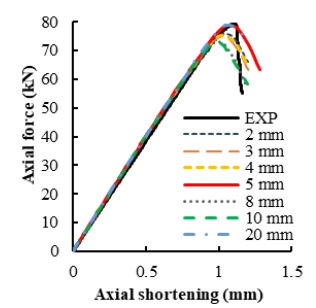


(a) Axial capacity with different mesh sizes

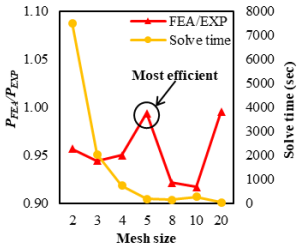


(b) Efficiency of FE models

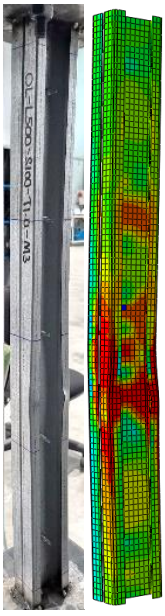


(c) Comparison of failure mode

**Fig. 10** Mesh convergence and independence study of OL series

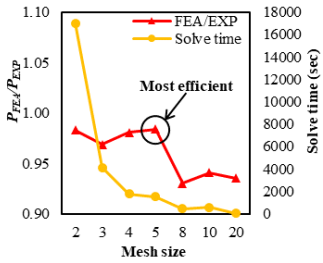


(a) MC3-140-A3

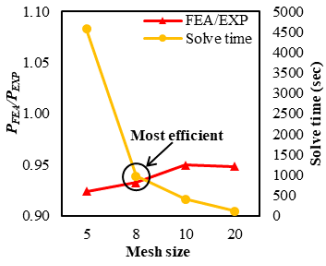


(b) LC3-140-A3

**Fig. 11** Mesh convergence and independence study of LU series

*3.3. Model validations*

The FE models were validated by comparing the axial capacities, axial shortening, out-of-plane deformation, and failure modes obtained between the experimental and FEA results. All developed FE models show strong agreement in simulating the actual behaviour for each series. The FEA results fell within the upper and lower boundaries of experimental results which are shown in Figs. 12 and 13. For the LU series, a comparison between the out-of-plane deformation of experimental and numerical results was not performed as the relevant data was not reported. Nevertheless, the failure modes of the model matched the actual behaviours closely. A summary of the comparisons of the axial capacities, axial shortening, and out-of-plane deformation of experimental and numerical results at yield, ultimate, and failure points was presented in Table 3.

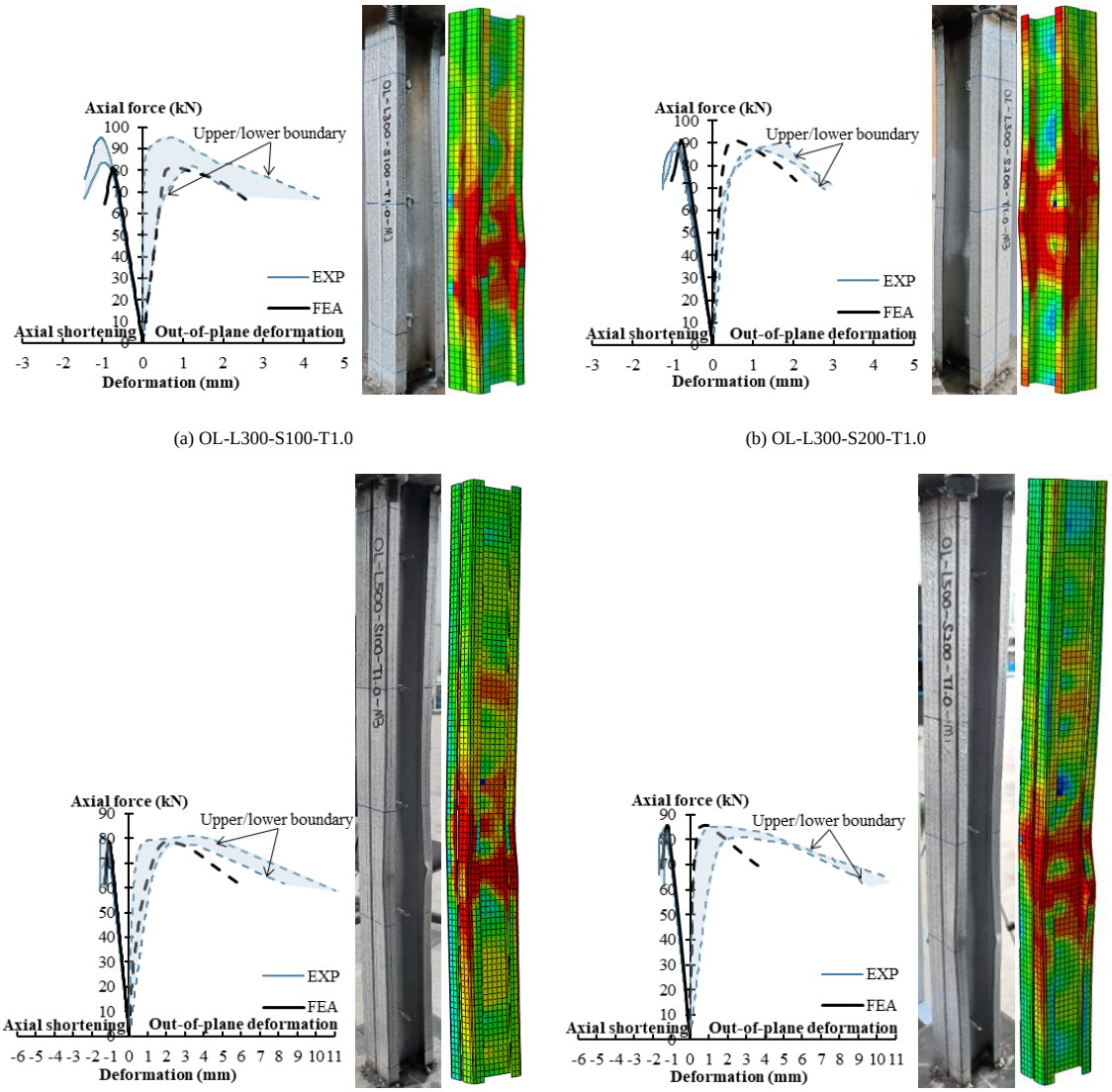


(a) OL-L300-S100-T1.0

(b) OL-L300-S200-T1.0

(c) OL-L500-S100-T1.0

(d) OL-L500-S200-T1.0

**Fig. 12** Model validation of OL series

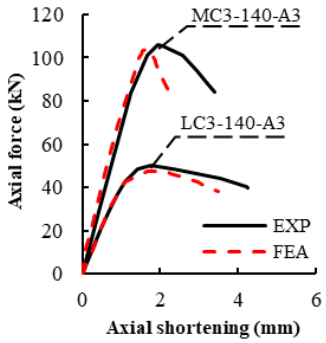


**Fig. 13** Model validation of LU series

**Table 3**
Comparisons of experimental and numerical results

| OL-L300-S100-T1.0-M2 | | | | | | | | | |
|---|---|---|---|---|---|---|---|---|---|
| | Force (kN) | | | Axial shortening (mm) | | | Out-of-plane deformation (mm) | | |
| | EXP | FEA | FEA/EXP | EXP | FEA | FEA/EXP | EXP | FEA | FEA/EXP |
| Yield | 72.32 | 78.17 | 1.08 | 0.74 | 0.68 | 0.92 | 0.68 | 0.54 | 0.79 |
| Ultimate | 83.63 | 81.26 | 0.97 | 0.96 | 0.74 | 0.77 | 1.76 | 0.77 | 0.44 |
| Failure | 66.86 | 64.69 | 0.97 | 1.46 | 0.94 | 0.64 | 4.36 | 2.68 | 0.61 |
| OL-L300-S200-T1.0-M3 | | | | | | | | | |
| | Force (kN) | | | Axial shortening (mm) | | | Out-of-plane deformation (mm) | | |
| | EXP | FEA | FEA/EXP | EXP | FEA | FEA/EXP | EXP | FEA | FEA/EXP |

| | | | | | | | | | |
|---|---|---|---|---|---|---|---|---|---|
| Yield | 85.29 | 88.59 | 1.04 | 0.78 | 0.71 | 0.91 | 1.03 | 0.35 | 0.34 |
| Ultimate | 90.29 | 91.37 | 1.01 | 0.92 | 0.78 | 0.84 | 1.72 | 0.51 | 0.30 |
| Failure | 72.23 | 73.04 | 1.01 | 1.22 | 1.02 | 0.84 | 2.80 | 2.07 | 0.74 |
| OL-L500-S100-T1.0-M3 | | | | | | | | | |
| | | Force (kN) | | Axial shortening (mm) | | | Out-of-plane deformation (mm) | | |
| | EXP | FEA | FEA/EXP | EXP | FEA | FEA/EXP | EXP | FEA | FEA/EXP |
| Yield | 77.41 | 76.99 | 0.99 | 1.04 | 0.99 | 0.95 | 0.67 | 1.61 | 2.42 |
| Ultimate | 79.32 | 78.83 | 0.99 | 1.11 | 1.08 | 0.98 | 1.28 | 2.23 | 1.74 |
| Failure | 63.43 | 61.51 | 0.97 | 1.15 | 1.30 | 1.14 | 8.34 | 5.99 | 0.72 |
| OL-L500-S200-T1.0-M1 | | | | | | | | | |
| | | Force (kN) | | Axial shortening (mm) | | | Out-of-plane deformation (mm) | | |
| | EXP | FEA | FEA/EXP | EXP | FEA | FEA/EXP | EXP | FEA | FEA/EXP |
| Yield | 81.72 | 84.83 | 1.04 | 1.20 | 1.19 | 0.99 | 0.61 | 0.49 | 0.81 |
| Ultimate | 85.12 | 85.70 | 1.01 | 1.30 | 1.22 | 0.94 | 1.28 | 0.70 | 0.55 |
| Failure | 61.52 | 61.32 | 1.00 | 1.37 | 1.68 | 1.22 | 9.37 | 5.40 | 0.58 |
| MC3-140-A3 | | | | | | | | | |
| | | Force (kN) | | Axial shortening (mm) | | | Out-of-plane deformation (mm) | | |
| | EXP | FEA | FEA/EXP | EXP | FEA | FEA/EXP | EXP | FEA | FEA/EXP |
| Yield | 100.94 | 97.55 | 0.97 | 1.59 | 1.37 | 0.86 | - | - | - |
| Ultimate | 105.80 | 104.07 | 0.98 | 1.94 | 1.66 | 0.86 | - | - | - |
| Failure | 84.06 | 81.70 | 0.97 | 3.40 | 2.28 | 0.67 | - | - | - |
| LC3-140-A3 | | | | | | | | | |
| | | Force (kN) | | Axial shortening (mm) | | | Out-of-plane deformation (mm) | | |
| | EXP | FEA | FEA/EXP | EXP | FEA | FEA/EXP | EXP | FEA | FEA/EXP |
| Yield | 45.94 | 42.65 | 0.93 | 1.27 | 1.17 | 0.92 | - | - | - |
| Ultimate | 50.20 | 47.67 | 0.95 | 1.79 | 1.87 | 1.05 | - | - | - |
| Failure | 40.00 | 38.13 | 0.95 | 4.24 | 3.48 | 0.82 | - | - | - |

**Table 4**
Proposed parametric matrix for slenderness ratio

| Classification | | Specimen no. | *L* | *a* | $(KL/r)_m$ |
|---|---|---|---|---|---|
| Short | OL series with 100 mm screw spacing | OL-L300-S100-1 | 300 | 100 | 33.55 |
| Intermediate | | OL-L500-S100-1 | 504 | 100 | 52.77 |
| | | OL-L700-S100-1 | 700 | 100 | 72.62 |
| | | OL-L900-S100-1 | 900 | 100 | 92.70 |
| Slender | | OL-L1100-S100-1 | 1100 | 100 | 112.88 |
| | | OL-L1300-S100-1 | 1300 | 100 | 133.11 |
| | | OL-L1500-S100-1 | 1500 | 100 | 153.39 |
| Short | OL series with 200 mm screw spacing | OL-L300-S200-1 | 300 | 200 | 41.26 |
| Intermediate | | OL-L500-S200-1 | 504 | 200 | 57.98 |
| | | OL-L700-S200-1 | 700 | 200 | 76.49 |
| | | OL-L900-S200-1 | 900 | 200 | 95.76 |
| Slender | | OL-L1100-S200-1 | 1100 | 200 | 115.40 |
| | | OL-L1300-S200-1 | 1300 | 200 | 135.26 |
| | | OL-L1500-S200-1 | 1500 | 200 | 155.25 |
| Short | LU series with 100 mm screw spacing | LU-L600-S100-2 | 600 | 100 | 31.60 |
| Intermediate | | LU-L1000-S100-2 | 1000 | 100 | 51.95 |
| | | LU-L1400-S100-2 | 1400 | 100 | 72.46 |
| | | LU-L1800-S100-2 | 1800 | 100 | 93.01 |
| Slender | | LU-L2200-S100-2 | 2200 | 100 | 113.59 |
| | | LU-L2500-S100-2 | 2500 | 100 | 133.42 |
| | | LU-L2900-S100-2 | 2900 | 100 | 154.72 |
| Short | LU series with 200 mm screw spacing | LU-L600-S200-2 | 600 | 200 | 33.55 |
| Intermediate | | LU-L1000-S200-2 | 1000 | 200 | 53.16 |
| | | LU-L1400-S200-2 | 1400 | 200 | 73.33 |
| | | LU-L1800-S200-2 | 1800 | 200 | 93.69 |
| Slender | | LU-L2200-S200-2 | 2200 | 200 | 114.15 |
| | | LU-L2500-S200-2 | 2500 | 200 | 133.93 |
| | | LU-L2900-S200-2 | 2900 | 200 | 155.15 |

### *3.4. Parametric study*

A parametric study was conducted to further study the axial behaviour of the CFS built-up sections with smaller $(w/t)_{max}$. To ensure the consistency of FE models and to make a fair comparison between parametric models, the verified models, OL-L500-S100, and LC3-140-A3 were selected for the parametric studies. In all parametric models, the $(w/t)_{max}$ of the OL and LU series was kept constant at 42.95 and 91.03 respectively to omit the influence of sectional slenderness on the axial capacity of CFS open built-up sections. The parameters studied were: (1) modified slenderness ratio, $(KL/r)_m$ and (2) screw arrangement for members with different section slenderness, $(w/t)_{max}$. The details of parametric models were summarised in Tables 4 and 5, each model was given a specimen number according to the series name, member length, screw spacing, and screw arrangement. Moreover, the parametric study on screw arrangement was only carried out for the FE models with an axial capacity closest to the mean capacity for each class (short, intermediate, and slender member).

**Table 5**
Proposed parametric matrix for screw arrangement

| Specimen no. | *L* (mm) | *a* (mm) | $(KL/r)_m$ | Screw arrangement |
|---|---|---|---|---|
| OL-L300-S100-2 | 300 | 100 | 33.55 | Double rows |
| OL-L700-S100-2 | 700 | 100 | 72.62 | Double rows |
| OL-L1500-S100-2 | 1500 | 100 | 153.39 | Double rows |
| OL-L300-S200-2 | 300 | 200 | 41.26 | Double rows |
| OL-L700-S200-2 | 700 | 200 | 76.49 | Double rows |
| OL-L1500-S200-2 | 1500 | 200 | 155.25 | Double rows |
| LU-L600-S100-1 | 600 | 100 | 31.60 | Single row |
| LU-L1800-S100-1 | 1800 | 100 | 93.01 | Single row |
| LU-L2900-S100-1 | 2900 | 100 | 154.72 | Single row |
| LU-L600-S200-1 | 600 | 200 | 33.55 | Single row |
| LU-L1800-S200-1 | 1800 | 200 | 93.69 | Single row |
| LU-L2900-S200-1 | 2900 | 200 | 155.15 | Single row |

## 4. Result analysis and discussion

### *4.1. Effect of slenderness ratio*

Results show that the OL series can achieve greater buckling resistance

when the member slenderness is less than 90 while the LU series can perform better when the slenderness increases as shown in Table 6 and Fig. 14. Besides, different buckling modes were observed for members with the same slenderness ratio but different section slenderness, especially for intermediate columns. The OL series was dominated by global buckling at the ultimate load followed by an interactive local-distortional-global buckling at the failure point. This was because the decrease in section slenderness restricted the occurrence of local and distortional buckling at the ultimate point. For the LU series, failure modes observed were interactive local-distortional buckling at the ultimate load and interactive local-distortional-global buckling at the failure point as reported in [10]. Apart from that, the OL series has greater structural integrity since they were more deformable and degraded gradually compared to the LU series when the member was slender.

**Table 6**
Summary of axial capacity with different slenderness ratios

| Specimen | $P_y$ (kN) | $\Delta_y$ (mm) | $P_u$ (kN) | $\Delta_u$ (mm) | $P_u/f_uA_g$ | Buckling mode | |
|---|---|---|---|---|---|---|---|
| | | | | | | Ultimate | Failure |
| S100 Series | | | | | | | |
| OL-L300-S100-1 | 73.31 | 0.71 | 87.47 | 0.83 | 0.67 | L | LD |
| OL-L500-S100-1 | 66.43 | 0.99 | 78.83 | 1.08 | 0.60 | LD | LDG |
| OL-L700-S100-1 | 47.87 | 1.00 | 56.71 | 1.12 | 0.44 | G | LDG |
| OL-L900-S100-1 | 28.94 | 0.76 | 40.72 | 1.18 | 0.31 | G | LDG |
| OL-L1100-S100-1 | 22.78 | 0.76 | 26.51 | 0.95 | 0.20 | G | LDG |
| OL-L1300-S100-1 | 17.10 | 0.68 | 20.37 | 0.81 | 0.16 | G | LDG |
| OL-L1500-S100-1 | 12.14 | 0.60 | 16.05 | 0.71 | 0.12 | G | G |
| LU-L600-S100-2 | 119.40 | 0.63 | 132.81 | 0.83 | 0.50 | LD | LD |
| LU-L1000-S100-2 | 111.87 | 0.98 | 124.54 | 1.27 | 0.46 | LD | LD |
| LU-L1400-S100-2 | 103.34 | 1.25 | 114.34 | 1.60 | 0.43 | LD | LDG |
| LU-L1800-S100-2 | 92.93 | 1.46 | 98.86 | 1.76 | 0.37 | LD | LDG |
| LU-L2200-S100-2 | 70.91 | 1.40 | 75.02 | 1.68 | 0.28 | LD | LDG |
| LU-L2500-S100-2 | 66.11 | 1.50 | 68.09 | 1.73 | 0.25 | G | G |
| LU-L2900-S100-2 | 52.14 | 1.66 | 52.24 | 1.82 | 0.20 | G | G |
| S200 series | | | | | | | |
| OL-L300-S200-1 | 73.31 | 0.71 | 83.89 | 0.77 | 0.64 | L | LD |
| OL-L500-S200-1 | 66.43 | 0.99 | 75.97 | 1.03 | 0.58 | LD | LDG |
| OL-L700-S200-1 | 47.87 | 1.00 | 61.55 | 1.23 | 0.47 | G | LDG |
| OL-L900-S200-1 | 28.94 | 0.76 | 37.87 | 1.18 | 0.29 | G | LDG |
| OL-L1100-S200-1 | 22.78 | 0.76 | 26.33 | 1.03 | 0.20 | G | LDG |
| OL-L1300-S200-1 | 17.10 | 0.68 | 20.06 | 0.87 | 0.15 | G | LDG |
| OL-L1500-S200-1 | 12.14 | 0.60 | 15.97 | 0.71 | 0.12 | G | G |
| LU-L600-S200-2 | 117.03 | 0.67 | 124.76 | 0.80 | 0.47 | LD | LD |
| LU-L1000-S200-2 | 112.99 | 1.08 | 120.03 | 1.35 | 0.45 | LD | LD |
| LU-L1400-S200-2 | 101.41 | 1.36 | 106.18 | 1.51 | 0.40 | LD | LDG |
| LU-L1800-S200-2 | 85.90 | 1.49 | 92.42 | 1.71 | 0.34 | LD | LDG |
| LU-L2200-S200-2 | 65.88 | 1.40 | 75.09 | 1.79 | 0.28 | LD | LDG |
| LU-L2500-S200-2 | 66.41 | 1.66 | 66.84 | 1.76 | 0.25 | G | G |
| LU-L2900-S200-2 | 51.80 | 1.66 | 51.86 | 1.82 | 0.19 | G | G |

Note: D = distortional buckling, LD = interactive local-distortional buckling, LDC = interactive local-distortional buckling with crushing, LDG = interactive local-distortional-global buckling.

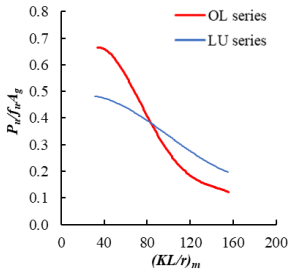


**Fig. 14** Parametric study on slenderness ratio

### *4.2. Effect of screw arrangement*

Based on the results in Section 4.1, OL-L300, OL-L700, OL-L1500, LU-L600, LU-L1800, and LU-L2900 were chosen to examine the effect of screw arrangement as summarised in Table 5. The effects of the screw arrangement were summarised in Table 7 and Fig. 15. Results show that the enhancement of the axial capacity is relatively more significant for short columns with greater section slenderness but minimal for intermediate and slender columns, especially for OL series as reported by [13]. This is because the proposed sections have a more compact design due to the reduced $(w/t)_{max}$ therefore, a single row screw is sufficient to form the built-up sections.

**Table 7**
Summary of axial capacity with different screw arrangement

| Specimen no. | $P_{FEA}$ | | $P_{FEA\_double}/P_{FEA\_single}$ |
|---|---|---|---|
| | Single row screws | Double rows screws | |
| OL-L300-S100 | 87.47 | 90.44 | 1.03 |
| OL-L700-S100 | 56.71 | 56.94 | 1.00 |
| OL-L1500-S100 | 16.05 | 16.09 | 1.00 |
| OL-L300-S200 | 83.89 | 91.99 | 1.10 |
| OL-L700-S200 | 61.55 | 56.02 | 0.91 |
| OL-L1500-S200 | 15.97 | 16.09 | 1.01 |
| LU-L600-S100 | 120.49 | 132.81 | 1.10 |
| LU-L1800-S100 | 89.99 | 98.86 | 1.10 |
| LU-L2900-S100 | 51.96 | 52.24 | 1.01 |
| LU-L600-S200 | 121.25 | 124.76 | 1.03 |
| LU-L1800-S200 | 89.19 | 92.42 | 1.04 |
| LU-L2900-S200 | 51.50 | 51.86 | 1.01 |
| | | Mean | 1.03 |
| | | SD | 0.05 |
| | | COV | 0.05 |

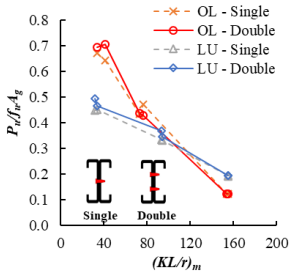


**Fig. 15** Parametric study on screw arrangement

### *4.3. Cost efficiency*

The reduction of $(w/t)_{max}$ was expected to enhance the buckling resistance of CFS sections yet provide a more cost-efficient design. To examine the cost efficiency of the proposed sections, the ultimate axial capacity was divided by the mass of steel materials for each investigated specimen for both the OL and LU series. The mass of steel was calculated by multiplying the density of steel

materials (7850 kg/m$^3$) with the cross-sectional area and length of the sections ($A_g \times L$). This is to identify the ability of the CFS sections to contribute to the axial capacity per unit weight. As shown in Fig. 16, the OL series is comparatively more cost-effective by achieving higher axial capacity while being relatively lighter in weight. However, the differences between the OL and LU series are getting closer for the slender members but still provide a better cost-performance ratio.

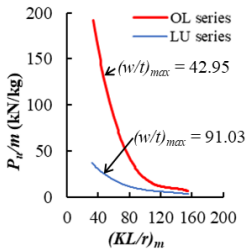


**Fig. 16** Comparison of cost efficiency

## 5. Conclusion

Experimental testing and numerical simulation were performed to study the axial behaviour of the proposed CFS open lipped built-up columns (OL series) which were designed with a $(w/t)_{max}$ less than 45, beyond the common range investigated in previous studies. The axial performance of the proposed sections was compared with the LU series which is the common size of CFS built-up sections reported in [10]. This study found that:

- For columns with a $(KL/r)_m$ less than 90, the OL series demonstrated better performance in achieving higher normalised axial capacity compared to the LU series.
- A single row screw is sufficient to provide good coupling between the CFS built-up members for sections with $(w/t)_{max}$ less than 45.
- OL series are more cost-efficient compared to LU series, attributed to its compact cross-sectional design featuring a smaller gross area.

## Acknowledgements

The authors would like to thank ASTEEL Sdn. Bhd. and the Ministry of Higher Education Malaysia under the Fundamental Research Grant Scheme (FRGS) with the grant number FRGS/1/2023/TK01/SWIN/02/1 for their support in this project.

## References

[1] W. Yu., R.A. LaBoube, H. Chen, Cold-formed steel design, Wiley, Hoboken, 2020.
[2] L. Gardner, X. Yun, Description of stress-strain curves for cold-formed steels, Construction and Building Materials. 189 (2018) 527–538.
[3] FJ. Meza, J. Becque, I. Hajirasouliha, Experimental study of the cross-sectional capacity of cold-formed steel built-up columns, Thin-Walled Struct. 155 (2020) 106958.
[4] J.H. Zhang, B. Young, Numerical investigation and design of cold-formed steel built-up open section columns with longitudinal stiffeners, Thin-Walled Struct. 89 (2015) 178-191.
[5] S. Selvaraj, M. Madhavan, Design of cold-formed steel built-up columns subjected to local-global interactive buckling using direct strength method, Thin-Walled Struct. 159 (2021) 107305.
[6] C.C. Mei, A.L.Y. Ng, H.H. Lau, S.L. Toh, Applications of built-up sections in lightweight steel trusses, in: Proceedings of Sixth International Conference on Advances in Steel Structures (2009) 857-864.
[7] Y. Dai, K. Roy, Z. Fang, G.M. Raftery, K. Ghosh, J.B.P. Lim, A critical review of cold-formed built-up members: Developments, challenges, and future directions, Journal of Building Engineering. 76 (2023) 107255.
[8] H.H. Lau, T.C.H. Ting, An investigation of the compressive strength of cold-formed steel built-up I sections, in: Proceedings of Sixth International Conference on Advances in Steel Structures (2009) 441-449.
[9] H.D. Craveiro, L.P.C. Rodrigues, L. Laím, Buckling resistance of axially loaded cold-formed steel columns, Thin-Walled Struct. 106 (2016) 358-375.
[10] Y. Lu, T. Zhou, W. Li, H. Wu, Experimental investigation and a novel direct strength method for cold-formed built-up I-section columns, Thin-Walled Struct. 112 (2017) 125–139.
[11] T. C. H. Ting, K. Roy, H. H. Lau, J. B. P. Lim, Effect of screw spacing on behavior of axially loaded back-to-back cold-formed steel built-up channel sections, Advances in Structural Engineering. 21 (3) (2018) 474–487.
[12] T. Zhou, Y. Li, L. Ren, L. Sang, L. Zhang, Research on the elastic buckling of composite webs in cold-formed steel back-to-back built-up columns – Part I: Experimental and numerical investigation, Structures. 30 (2011) 115-133.
[13] S.T. Vy, M. Mahendran, DSM design of fixed-ended slender built-up back-to-back cold-formed steel compression members, J. Constr. Steel Res. 189 (2022) 107053.
[14] M. Abbasi, K.J.R. Rasmussen, M. Khezri, B.W. Schafer, Experimental investigation of the sectional buckling of built-up cold-formed steel columns, J. Constr. Steel Res. 203 (2023) 107803.
[15] Y. Cui, J. Zhang, C. Ma, M. Niu, K. Jiang, S. Li, A. Su, Testing, numerical modelling and design of G550 high strength cold-formed steel built-up section columns, Thin-Walled Struct. 196 (2024) 111529.
[16] AS/NZS. Cold-formed steel structures, AS/NZS 4600: 2018, Standards Australia and Standards New Zealand, Sydney, Australia, 2018.
[17] AS, Metallic Materials-Tensile Testing-Method of test at room temperature, AS 1391, Standards Australia, Sydney, Australia, 2020.
[18] Y. Huang, B. Young, The art of coupon tests, J. Constr. Steel Res. 96 (2014) 159–175.
[19] R. Park, Evaluation of ductility of structures and structural assemblages from laboratory testing, Bulletin of the New Zealand National Society for Earthquake Engineering. 22 (3) (1989) 155-166.
[20] AISI, North American Specification for the Design of Cold-Formed Steel Structural Members, AISI S100-16, American Iron and Steel Institute, Washington, DC, 2016.
[21] ABAQUS, (2017). Abaqus User Manual, Simulia, Dassault Systèmes, Providence, RI, 2017.
[22] K.H. Nip, L. Gardner, A.Y. Elghazouli, Cyclic testing and numerical modelling of carbon steel and stainless steel tubular bracing members, Eng Struct. 32 (2010) 424-441.
[23] D.A. Padilla-Llano, C.D. Moen, M.R. Eatherton, Cyclic axial response and energy dissipation of cold-formed steel framing members, Thin-Walled Struct. 78 (2014) 95-107.